Bioactive Materials 12 (2022) 64–70

Contents lists available at ScienceDirect

Bioactive Materials

journal homepage: www.keaipublishing.com/en/journals/bioactive-materials

Improving the radiopacity of Fe–Mn biodegradable metals by magnetron-sputtered W–Fe–Mn–C coatings: Application for thinner stents

Samira Ravanbakhsh [a,b], Carlo Paternoster [a], Gianni Barucca [c], Paolo Mengucci [c], Sofia Gambaro [d], Theophraste Lescot [b,e], Pascale Chevallier [a], Marc-André Fortin [b,e,f], Diego Mantovani [a,*]

[a] Laboratory for Biomaterials and Bioengineering, Canada Research Chair I in Biomaterials and Bioengineering for the Innovation in Surgery, Department of Min-Met-Materials Engineering, Research Center of CHU de Quebec, Division of Regenerative Medicine, Laval University, Quebec City, Quebec G1V 0A6, Canada
[b] Laboratory for Biomaterials in Imaging (BIM), Axe Médecine Régénératrice, Centre Hospitalier Universitaire (CHU) de Québec - Université Laval, 2705, boul. Laurier (T1-61a), Québec, G1V 4G2, Canada
[c] Department of Materials, Environmental Sciences and Urban Planning, Università Politecnica delle Marche, via Brecce Bianche 12, 60131, Ancona, Italy
[d] National Research Council, Institute of Condensed Matter Chemistry and Energy, CNR-ICMATE, Via de Marini 6, 16149, Genova, Italy
[e] Département de Génie des Mines, de la Métallurgie et des Matériaux, Centre de Recherche sur les Matériaux Avancés (CERMA); Université Laval, Québec, G1V 0A6, Canada
[f] Axe Médecine Régénératrice, Centre Hospitalier Universitaire (CHU) de Québec - Université Laval, 2705, boul. Laurier (T1-61a), Québec, G1V 4G2, Canada

ARTICLE INFO

Keywords:
Fe–Mn-Based alloys
Degradable coatings
W–Fe–Mn–C coatings
Magnetron sputtering
Radiopacity
Stent fluoroscopy

ABSTRACT

In this exploratory work, micrometric radiopaque W–Fe–Mn–C coatings were produced by magnetron sputtering plasma deposition, for the first time, with the aim to make very thin Fe–Mn stents trackable by fluoroscopy. The power of Fe–13Mn-1.2C target was kept constant at 400 W while that of W target varied from 100 to 400 W producing three different coatings referred to as *P*100, *P*200, *P*400. The effect of the increased W power on coatings thickness, roughness, structure, corrosion behavior and radiopacity was investigated. The coatings showed a power-dependent thickness and W concentration, different roughness values while a similar and uniform columnar structure. An amorphous phase was detected for both *P*100 and *P*200 coatings while γ-Fe, bcc-W and W_3C phases found for *P*400. Moreover, *P*200 and *P*400 showed a significantly higher corrosion rate (CR) compared to *P*100. The presence of W, W_3C as well as the Fe amount variation determined two different micro-galvanic corrosion mechanisms significantly changing the CR of coatings, 0.26 ± 0.02, 59.68 ± 1.21 and 59.06 ± 1.16 μm/year for *P*100, *P*200 and *P*400, respectively. Sample *P*200 with its most uniform morphology, lowest roughness (RMS = 3.9 ± 0.4 nm) and good radiopacity (~6%) appeared the most suitable radiopaque biodegradable coating investigated in this study.

1. Introduction

Biodegradable metals, a new class of biomaterials, are promising in stenting applications. Cardiac biodegradable stents have to sustain coronary vessels as long as required and then degrade being catabolized by physiological pathways [1]. These tiny devices also require to be visible during their implantation. In fact, cardiac stents, tiny expandable devices mounted on a balloon catheter, are inserted into a vein, and guided under fluoroscopy imaging toward the diseased segment of the coronary vessel. Magnesium, zinc and iron-based alloys have been investigated as potential metals for biodegradable stents [2]. Today, only one biodegradable metal stent has been commercialized in Europe, fabricated from a Mg alloy [3]. In this device, two tantalum markers are inserted on the extremities of the stent to position the stent under X-ray irradiation [4]. However, tantalum is corrosion-resistant; thus, its fate upon degradation of the stent in the body is unclear and raises concern. Other works used different approaches to increase the radiopacity of NiTi stents. For instance, addition of 10 wt% of W [5] was revealed as a valid approach, as well as the application of sputtered 5–10 μm Ta coatings on NiTi surfaces [6]. In these studies, the Ta and W materials

Peer review under responsibility of KeAi Communications Co., Ltd.
* Corresponding author. Laboratory for Biomaterials and Bioengineering, CRC-I, Axe Médecine Régénératrice, Centre Hospitalier Universitaire (CHU) de Québec - Université Laval, 10 rue de l'Espinay, Québec, G1L 3L5, Canada.
E-mail address: diego.mantovani@gmn.ulaval.ca (D. Mantovani).

https://doi.org/10.1016/j.bioactmat.2021.10.022
Received 24 October 2020; Received in revised form 1 May 2021; Accepted 18 October 2021
Available online 26 October 2021

exhibited a much higher visibility in X-ray images compared with bare NiTi stents.

Fe–Mn–C are biodegradable alloys characterized by a high level of formability and acceptable corrosion properties compared to the Mg alloys currently used for biodegradable metal stents [7]. Fe–Mn–C alloys are ductile and they have a high yielding strength ($\sigma_Y \approx 620$ MPa) which make them promising candidates for the fabrication of thin degradable stents. This could yield to considerable improvements at the clinical implantation step [8]. However, the radiopacity of Fe–Mn–C alloys to the X-rays used in interventional fluoroscopy (30–80 keV) and in CT-scanning is low (e.g. $\rho = 7.72$–7.59 g cm^{-3}; $\mu/\rho = \sim 1.50$–1.81 cm^2 g^{-1} at 50 keV), if compared to more electron-dense alloys (e.g. Co–Cr, $\rho = 9.27$ g cm^{-3}, $\mu/\rho = 2.58$ cm^2 g^{-1} at 50 keV) [9,10]. As a result, inadequate visibility in fluoroscopy is a major drawback of Fe–Mn–C stents, especially for thinner devices. Fluoroscopy is a real-time X-ray-imaging technology used during the implantation, whereas CT-scan is an X-ray based three-dimensional imaging technique used effectively for the post-surgery follow-up of the device. Therefore, one promising strategy to improve the radiopacity of Fe–Mn–C alloys is to enrich them with radiopaque elements [11] such as tungsten (W).

Tungsten is a high-density (19.30 g cm^{-3}) biodegradable element, with a relatively greater X-ray attenuation coefficient (5.94 and 7.81 cm^2 g at 50 keV and 80 keV, respectively), compared to both Fe (1.95 and 0.59 cm^2 g at 50 keV and 80 keV, respectively), and Mn (1.71 and 0.53 cm^2 g at 50 keV and 80 keV, respectively) [10–12]. The radiopacity of biodegradable Fe–Mn–C devices could be improved by adding W-rich coatings, provided these coatings could also biodegrade within a few months (typically 6) after implantation. The novelty and impact of the proposed approach resides in the development of new and advanced radiopaque coatings providing visibility of the whole stent, and not only at the two extremities such as with the Ta markers integrated in current Mg stents.

The present study is based on the hypothesis that a Fe–Mn–C foil (or wire) coated with a W-rich radiopaque coating, could present similar corrosion properties as the base metal (Fe–Mn–C), while providing a functional radio-visibility for X-ray interventional fluoroscopy and CT imaging. Among several deposition techniques, plasma-based magnetron sputtering was selected for its potential to deposit a uniform, highly adhesive and strongly cohesive coating by tuning several deposition parameters such as sputtering power, pressure of the chamber during the deposition and temperature of the substrate [13]. In this study, several W–Fe–Mn–C coatings were obtained using co-deposition of W and Fe–Mn–C targets by the magnetron sputtering technique. The amount of W in the coatings was varied between ~45 at.% and ~87 at.% by using sputtering powers applied to the W target from 100W to 400W. The effect of chemical composition on the physiochemical and electrochemical properties of W–Fe–Mn–C coatings was investigated by several characterization techniques. Finally, radiopacity of the coatings, was measured by a micro-CT scanner (2D projections as for fluoroscopy).

2. Materials and methods

2.1. Substrates

For the chemical composition, structure and corrosion characterization studies, coatings were deposited on Silicon wafers (CZP<100>, Universitywafer Inc., MA, USA). Silicon was selected as the reference substrate to assess microstructure, phase structure, thickness, roughness, as well as corrosion behaviour of W–Fe–Mn–C coatings. This system allowed a preliminary characterization of the coatings features, e.g. an easily assignment of the XRD reflexes and an accurate assessment of coating thickness. Pure Fe foil (99.99%, 50 ± 5 μm, Goodfellow, USA) was instead selected as substrate to study the radiopacity of the same coatings since both thickness and attenuation coefficient of Fe are close to those of thin biodegradable stent wiring. Future studies envisage to assess radiopaque coating depositions on Fe-based 3D materials to consider both the real substrate surface features and its more complex geometry.

2.2. Coating process

The magnetron sputtering deposition system, equipped with radio-frequency (RF) and pulsed DC power supplies, was used to perform depositions with a double target system (Plasmionique MS300, Varennes, QC, Canada). DC power source was used for the sputtering a tungsten (W) target, whereas RF power source was used for the Fe–13Mn-1.2C target (Hadfield steel from Polstar Steel, Mississauga, ON, Canada). The base pressure was $\sim 1 \times 10^{-6}$ Torr before starting the deposition. An Ar (99.9%) working pressure (P_W) of 20 mTorr, and a deposition time of 60 min were kept throughout the deposition procedures. The sample holders were set at a distance of 10 cm from the center of the targets. Both targets were set at an angle of 30° with center line of the sample holder. A sputtering power of 400 W was applied on the Fe–13Mn-1.2C target while three different powers (100, 200, 400 W) were applied on the W target in order to vary the chemical compositions of coatings. Since only the tungsten power was varied, samples are referred to as *P*100, *P*200, and *P*400 (where the numbers indicate the power values adopted for tungsten deposition).

2.3. Characterization

Microstructural characterizations of surfaces and cross-sections of samples were conducted by Scanning Electron Microscopy (SEM) performed with a FEI Quanta250 SEM system (Thermo-Fisher, OR, USA) using a secondary electron detector. The SEM images were acquired with an acceleration voltage of 15 kV. Topography and roughness of the samples were investigated by Atomic Force Microscopy (AFM, Dimension™ 3100, Digital Instrument, CA, USA), operated in tapping mode. Elemental analysis of samples was carried out by a micro-X-ray fluorescence spectroscopy system (μ-XRF, Bruker, Tornado M4, USA) equipped with a rhodium (Rh) source and two detectors. The acquisitions were performed at E = 50 kV on 3 areas of 1×1 mm^2 for each sample. Crystallographic structure of the coating was assessed by X-ray Diffractometry (Siemens® D5000, graphite monochromator, Texas USA). Surface elemental analysis was performed by X-ray photoelectron spectrometry (PHI 5600-ci, Physical Electronic, MN, USA), with an achromatic Al X-ray source, at an incident angle of 45° and at a residual pressure of 8×10^{-9} Torr. The analyzed area was 0.5 mm^2, and survey spectra analyses were done in triplicate. Corrosion behavior was investigated by electrochemical tests at room temperature using a mini-cell system [14], in modified Hanks' solution, whose composition and preparation were reported elsewhere [15]. The open circuit potential (OCP) was recorded for 20 min followed by a potentiodynamic polarization (PDP) test at a scan rate of 0.166 mV/s, in the range - 0.5 to + 0.5 V. The corrosion rate (μm/year) was calculated according to the established protocol reported in Ref. [16]. Five samples per condition were used to investigate electrochemical properties. Statistical analyses and comparisons among groups were evaluated by one-way ANOVA with post hoc Tukey test to correct for multiple comparisons. Significance was retained when $p < 0.05$. Data are expressed as mean ± standard error of the mean.

2.4. Radiopacity

The radiopacity of W-rich coatings (1.8 and 4.5 μm thick) deposited on 50 μm-thin pure Fe foils, was measured with a X-ray computed micro tomography system (CT, eXplore Locus 80, GE Healthcare, Milwaukee, USA), operated with a W anode and by keeping a fixed angle (vertical 2D projections: "0" angle). The samples were embedded in gelatin type A (50 g/L in deionized water) and inserted in the CT scanner. The following imaging parameters were used: 60 and 80 kVp energies (tungsten anode tube voltage), 450 mA current, 100 ms detector

exposure time, 1 x 1 binning. Image visualization and signal measurements were performed on MicroView (Parallax Innovations version: 2.5.0, Ilderton, ON, Canada). Correlation of contrast to gray–scale value was calculated as follows [17]:

$$C = \frac{GSV_{coated} - GSV_{uncoated}}{GSV_{coated} + GSV_{uncoated}} \times 100 \quad (1)$$

where C is the contrast, GSV_{coated} and $GSV_{uncoated}$ are grayscale values of coated and uncoated samples for the 2D projected X-ray attenuation images acquired at "0" angle in the CT-scanner.

3. Results and discussion

Samples of the coated substrates were fractured. Both cross-sections and top-views were visualised in SEM (Fig. 1a–i). The coatings produced at three different sputtering powers (*P*100, *P*200 and *P*400; corresponding to the three different powers of 100, 200 and 400 *W*, respectively), had power-dependent thicknesses and W concentrations, while showing similar columnar structures (Fig. 1a–c). Thickness values of 0.9 ± 0.2 μm, 1.3 ± 0.1 μm and 1.8 ± 0.2 μm were found for *P*100, *P*200 and *P*400, respectively, (Fig. 1a–c). No evidence of cracking was found on the sample surfaces (Fig. 1d–f). In addition, both *P*100 and *P*200 samples showed a relatively uniform structure, whereas, in the case of *P*400 samples, a microstructure composed of two different morphologies was found (Fig. 1i): Pyramidal crystallites emerging from a smoother base were evident both from SEM and AFM analyses (Fig. 1i and l). In particular, AFM analysis (Figure 1l) clearly showed the microstructure typical of *P*400 samples where the height of the crystallites could be in the range of 50–60 nm. In fact, roughness values (RMS, 2 × 2 μm^2) of *P*100 (3.9 ± 0.4 nm) and *P*200 (6.1 ± 1.0 nm) did not significantly differ,

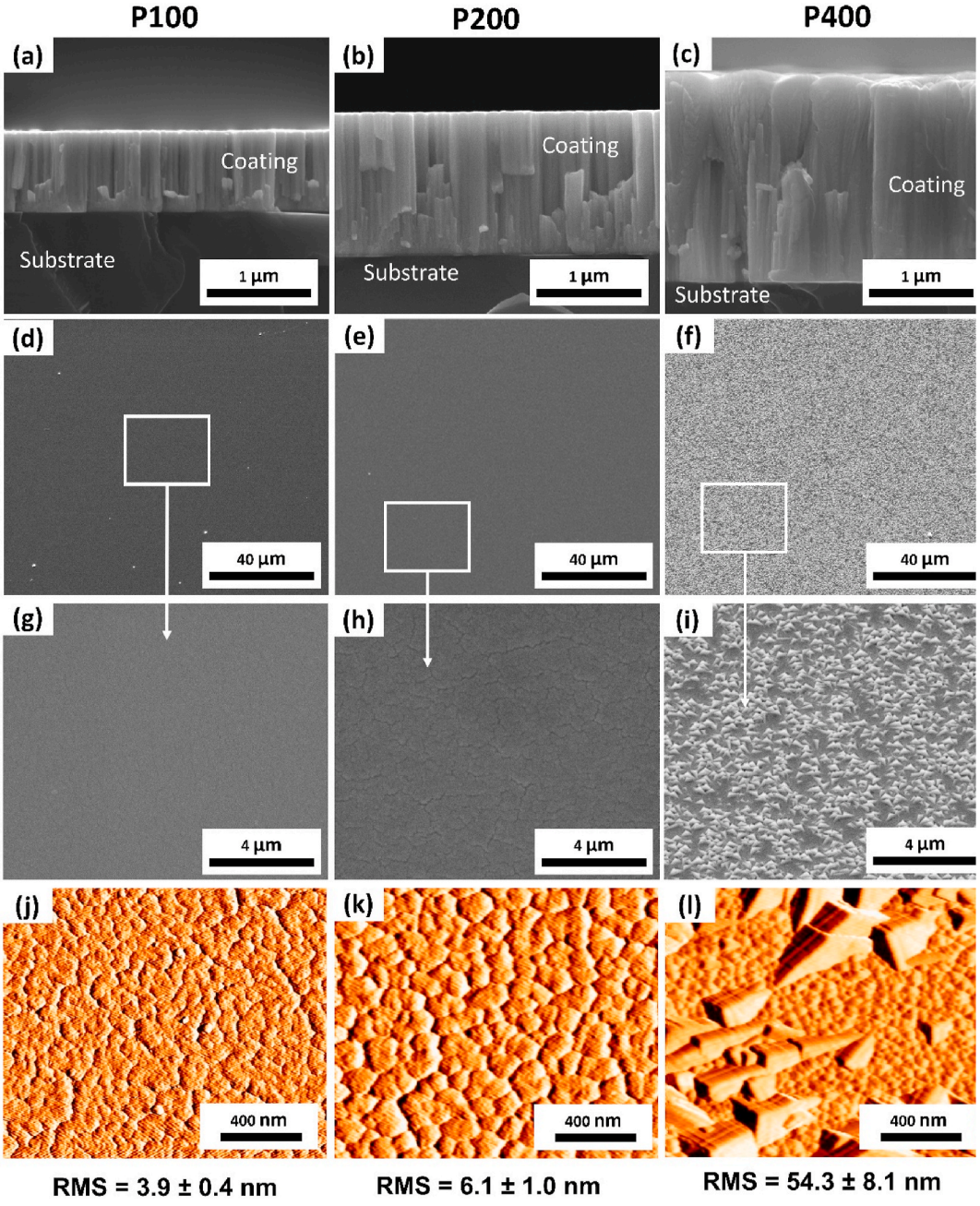

Fig. 1. *P*100, *P*200 and *P*400 coatings: (a–c) cross-sections of fractured coatings for 1 h of deposition visualised by SEM; (d–i) top views of the coatings; (j–l) AFM images and roughness measurements of the coatings (RMS, 2 × 2 μm^2).

while RMS increased up to 54.3 ± 8.1 nm for the coating obtained at the highest W sputtering power (*P*400). The differences observed in coating microstructures can be correlated to the amounts of tungsten and other elements in the coating deduced from XRF analysis (Table 1). Increasing the sputtering power during the deposition increased the W content (three times higher for *P*400 sample) while drastically decreased Fe and Mn amounts.

The effect of a higher amount of W on the crystallographic structure of the coatings was assessed by XRD measurements. The XRD patterns revealed for *P*100 and *P*200 coatings, did not show clear reflexes (Fig. 2b), with the exception of a wide reflection at $2\theta = 42°$, indicative of the presence of amorphous phase. In the *P*400 coating however, Bragg reflex corresponding to γ-Fe (111) and bcc W (110) were clearly observed. The presence of a reflex at $2\theta = \sim 37°$ was attributed to the formation of tungsten carbide (W_3C), which could be associated to the pyramidal structures found on the surface of the sample, as evidenced by SEM and AFM images (Fig. 1f and i). The presence of C in W coatings produced by sputtering, is known to promote the formation of W-rich metallic carbides [18]. Also, traces of γ-Fe ($2\theta = \sim 44°$) were deduced in the *P*400 sample XRD spectra, as Mn is well-known as a stabilizer of austenitic iron [2]. Furthermore, Fe can accelerate the formation of tungsten carbide [19].

XPS analyses of the samples and Fe–Mn–C target were shown in Fig. 3. The Mn/Fe weight ratio of Fe–13Mn-1.2C target used for sputtering was ~0.15. However, XPS results showed (Fig. 3) that on the outermost layer of the coating the Mn/Fe ratio varied from ~0.25, to0.5 and ~1.0 for *P*400, *P*100 and *P*200, respectively. Thus, the upper surface of the coatings (~5 nm) is richer in Mn, compared with the material of the sputtered target (Fe–13Mn-1.2C) and this independently from the power used to sputter the W target (100, 200, and 400 W). Both XPS (Fig. 3 and Table 2) and XRF (Table 1) analyses confirmed the increase of W in coatings along with the sputter power applied to the W target. As a result, the total amount of metallic elements ($\sum$ = W + Mn + Fe) on the surface increased from 16.96 ± 0.76 at. %, to 20.93 ± 1.13 at. %, and to 28.20 ± 0.92 at. % for *P*100, *P*200 and *P*400, respectively. However, the W/(W + Fe + Mn) ratio was 0.36 ± 0.02, 0.48 ± 0.3 and 0.81 ± 0.3 for *P*100, *P*200 and *P*400, respectively. By opposition, the Fe/(W + Fe + Mn) decreased at higher tungsten deposition power. Comparing Mn/Fe ratio of the surface of the coating with Fe–Mn–C target, it was noticed that P400 presented lower Mn/Fe ratio led to conclude that there is an Mn depletion for *P*400. In conclusion, the outermost surface of sample P400 showed a lower content of O1s and Mn2p3, higher content of W4f compared to other conditions. The difference in the chemical composition of surface of the coating at higher deposition power can strongly affect its corrosion behavior.

The corrosion behavior of the different samples was assessed by testing 5 samples per condition (Fig. 4). First, the OCP curves showed that after 600 s, all curves achieved a stabilization potential (Fig. 4a). However, the potential plateaus were different for the three considered conditions, showing a general decrease for higher amounts of W. In fact, samples *P*200 and *P*400 showed a potential shift to more negative values, indicating a higher electrochemical activity at their surface. Fig. 4b, displaying the potentiodynamic polarization curves of the coatings allowed to evaluate the corrosion current density (I_{corr}) and

Table 1
XRF results of elemental characterization of *P*100, *P*200 and *P*400 coatings.

Elements	*P*100		*P*200		*P*400	
	At. %	Wt. %	At. %	Wt. %	At. %	Wt. %
Fe	69.1 ± 0.4	47.3 ± 0.6	59.2 ± 0.5	34.2 ± 0.5	30.2 ± 0.4	11.8 ± 0.2
Mn	10.6 ± 0.1	7.1 ± 0.1	8.9 ± 0.1	5.1 ± 0.1	1.9 ± 0.1	0.7 ± 0.1
W	20.3 ± 0.4	45.6 ± 0.7	31.9 ± 0.5	60.7 ± 0.6	67.9 ± 0.3	87.5 ± 0.2

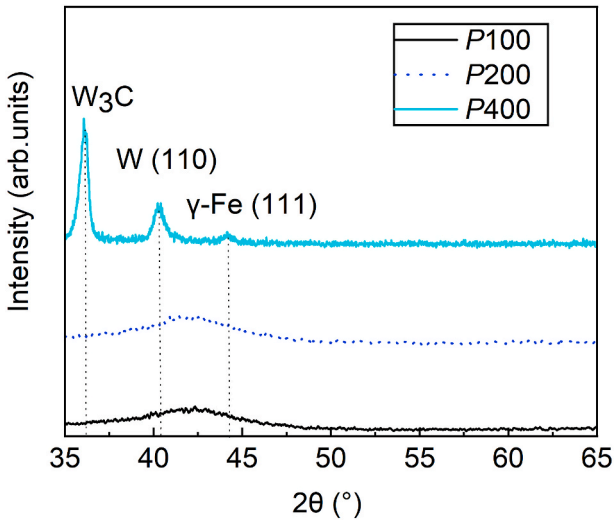

Fig. 2. X-ray diffraction patterns of *P*100, *P*200 and *P*400 coatings.

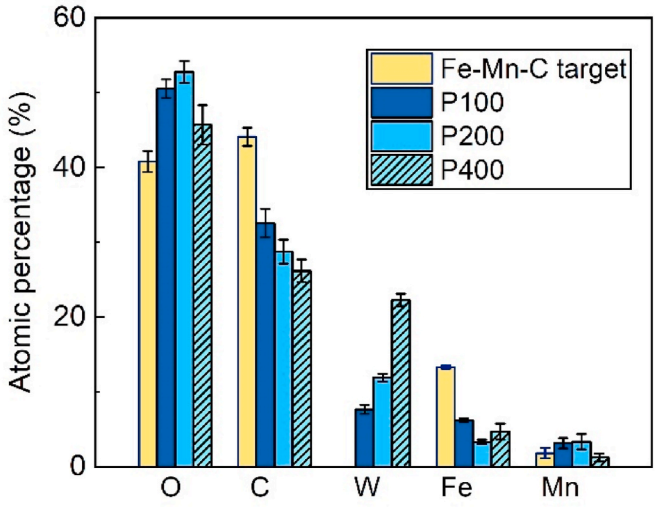

Fig. 3. (a) XPS survey results of the coatings. The amount of Fe, Mn and W were respectively calculated on the basis of Fe2p3, Mn2p3 and W4f orbitals.

Table 2
Relative amount of the metallic elements on the surface before Ar etching. ∑ is the sum of metallic components on the surface which are W4f, Fe2p3 and Mn2p3.

Elemental ratio	Target	Samples		
	Fe–Mn–C	*P*100	*P*200	*P*400
∑ = Fe + Mn + W [at. %]	15.10 ± 0.70	16.96 ± 0.76	20.93 ± 1.13	28.20 ± 0.92
Mn/Fe	0.13 ± 0.06	0.54 ± 0.04	1.02 ± 0.11	0.25 ± 0.05
Fe/∑	0.88 ± 0.05	0.44 ± 0.33	0.35 ± 0.04	0.16 ± 0.03
Mn/∑	0.12 ± 0.04	0.18 ± 0.04	0.16 ± 0.04	0.04 ± 0.02
W/∑	–	0.36 ± 0.01	0.48 ± 0.01	0.80 ± 0.03

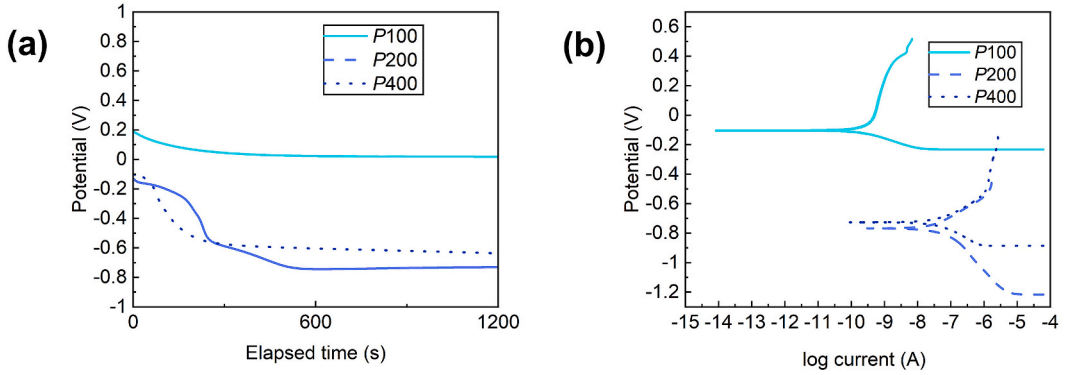

(c)

Sample	Corrosion current density (μA/cm²)	Corrosion potential (mV)	Corrosion rate (μm/year)
P100	0.04 ± 1.35	-100.76 ± 13.76	0.26 ± 0.02
P200	9.68 ± 0.26	-748.50 ± 12.42	59.68 ± 1.21
P400	10.96 ± 1.58	-697.19± 44.75	59.06 ±1.16

Fig. 4. (a) OCP vs immersion time in Hank's modified solution for samples P100, P200 and P400; (b) Potentiodynamic polarization curves of P100, P200 and P400 and (c) table of their electrochemical parameters.

corrosion rate (*CR*) [20]. The calculated CR, on the basis of Tafel extrapolation, increased drastically with increasing W sputtering powers from 0.26 ± 0.02 μm/year for *P100* to 59.6 ± 1.2 μm/year for *P*200 and 59.0 ± 1.1 μm/year for *P*400 sample. The results showed that there was no significant difference between CR of *P*200 and *P*400. Compared to the sample *P100*, it was possible to notice that the anodic curve of the samples *P*200 and *P*400 shifts to higher current density values, indicating a higher anodic dissolution of the metal. Increasing the corrosion rate could be related to the difference in the standard potential of W (−0.04 V), which was higher in comparison with that of pure iron (−0.44 V), and could be considered to act as a superior cathode [21]. In this case, W was functionalized as a cathode and the Fe acted as the

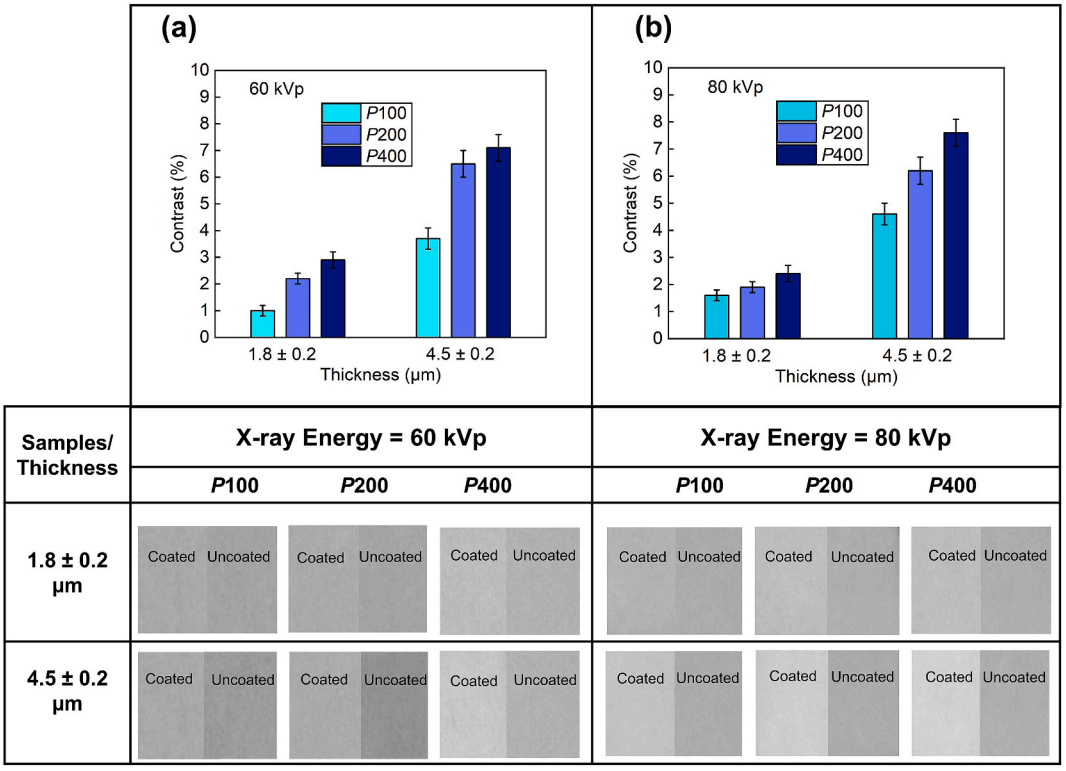

Fig. 5. Radiopacity results of 50 μm-thick Fe foils coated with W–Fe–Mn–C using 100, 200 and 400 W applied to the W sputter target (P100, P200 and P400 samples); the samples were CT-scanned at (a) 60 kVp and (b) 80 kVp (tungsten anode); images from which the contrast results were extracted, are inserted below each graph.

anode to generate micro-galvanic corrosion. Increasing the W amount increased the cathodic areas and micro-galvanic sites what could explain the highest corrosion rates. However, increasing the W amount did not increase the CR of *P*400 samples while *P*200 was more prone to corrosion compared to *P*400. It seems that both the presence of W_3C and the higher surface roughness of *P*400 sample have a dominant effect on the corrosion properties of this alloy rather than the effect of a higher amount of W. It was reported by Pradhan et al. that the depth of penetration of the corrosive solution increased with the surface roughness and the electron release rate was also significantly higher for a rougher surface. For this reason, coating CR increased with the real surface area [22]. Tungsten carbide increased the CR of the Fe-based alloy coating. However, increasing the mass fraction of the fragile tungsten carbide phase leads to holes and other defects that can increase the CR of coating [23].

Attenuation of X-rays by the coatings was measured by a microCT scanner with a tungsten anode X-ray tube operated at 60 kVp and 80 kVp. The results of these radiopacity tests are reported in Fig. 5. The 2D projection images, from which the contrast results were extracted (at "0" degree angle in the CT scanner), are inserted in Fig. 5. More radiopaque Fe foils were obtained by applying higher sputtering powers at the W target, which led also to thicker coatings. The maximum radiopacity was achieved for the *P*400 sample (4.5 ± 0.2 μm thick on a 50 μm-Fe foil), measured at 80 kVp, with a 7.6% contrast between coated and uncoated Fe foil. At 60 kVp the contrast measured for the *P*400 sample decreased to 7.1%, in spite of the presence of the k-edge of W at 69 keV. This very slight decrease in contrast between the 80 kVp and 60 kVp operation modes, reflects the broad range of the energy spectrum of photons produced by the tungsten anode tube. In fact, this range of photon energies is relatively similar to that observed in fluoroscopy systems in the stenting clinics. Interestingly, in the thinner coatings (1.8 ± 0.2 μm), and at the highest sputtering powers used for W (400 W), a decrease in contrast was observed by changing from 60 kVp to 80 kVp. Although the 80 kVp maximum tube energy is well above the k-edge of W, the amount of tungsten in the thin coatings in not sufficient to generate a significant attenuation effect. As a result, more photons pass through the coated Fe foils at 80 kVp compared with the 60 kVp condition, and thus lower contrasts are found at higher X-ray tube energies. Pure Fe has an attenuation coefficient of 1.205 cm^2/g at 60 keV, and 0.595 cm^2/g at 80 keV [10]. These findings were compared to the radiopacity of conventional Co–Cr (L605) stents. In this alloy, the presence of 15 wt% tungsten provides optimal visibility in fluoroscopy [24]. To increase the visibility of pure Fe foils, this weight percentage of tungsten should be integrated to thickness of the 50 ± 5 μm of Fe foils treated in the present study. The concentration of W achieved in the (4.5 ± 0.2 μm) coatings was 60.70 ± 0.06 wt % for *P*200 and 87.45 ± 0.06 wt% for *P*400. The thickness of the coatings represents 8.25% of the total section of the deposited substrates. The total weight percentage of W found in each one of the coatings, multiplied to the relative section of the coatings, points to an approximate weight concentration of 5.01 wt% and 7.22 wt% equivalent W in the deposited Fe substrates. Hence in order to reach the same level of X-ray visibility in Fe alloys imaged in fluoroscopy as that produced by 15 wt%. W in conventional CoCr alloys, the sputtered W–Fe–Mn–C coatings should be at least 2 or 3 times thicker. Therefore, based on the literature related to radiopaque coatings [6] and the results obtained in the present study W–Fe–Mn–C coatings at least 10 μm thick would be necessary to achieve visibility. In this light, 4–5 μm thick coatings can be applied on both sides of the Fe–Mn stents to provide optimum radiopacity. In the clinics, the efficient tracking of stents in fluoroscopy require the objects to be visualised at to contrast of at 300 Hounsfield unit (HU), while the contrast of blood containing iodine (contrast agent) is 200 HU [25,26]. The next step of this work will consist in developing 3D objects with a W-rich coating, for visualization in both fluoroscopy and X-ray CT-scanning. It should be mentioned that the geometry of the stent has an important effect on the coating thickness, columnar growth angle, and porosity. Therefore, in the next step of this work a comprehensive study will be done to put into evidence the effect of stent geometry on the properties of the coatings.

4. Conclusions

Micrometric coatings of W–Fe–Mn–C alloy were deposited on Si wafers and Fe-foils by magnetron co-sputtering of Fe–13Mn-1.2C and W. The increase of the sputtering power of *W* from 100 *W* to 400 *W* varied the W amount found on sample surfaces, from 45.6 ± 0.7 to 87.5 ± 0.2 wt%. SEM and AFM studies evidenced a change in the coatings thickness, morphology and roughness by increasing the amount of tungsten. Thickness values of 0.9 ± 0.2 μm, 1.3 ± 0.1 μm and 1.8 ± 0.2 μm were found for *P*100, *P*200 and *P*400, respectively. W_3C phase was found just in the *P*400 sample. The presence of W, W_3C, as well as the variation of Fe amount in the coating chemical composition, changed sample corrosion rate from 0.26 ± 0.02 to 59.68 ± 1.21 and 59.06 ± 1.16 μm/year. In particular, *P*200 and *P*400 showed a higher CR compared to *P*100. Two different kinds of micro-galvanic corrosion mechanism were found to increase the corrosion rate of *P*200 and *P*400. In the case of *P*400 both the higher roughness and the presence of W and W_3C as cathodic sites played an important role in increasing the CR of the coating. Sample *P*200 displayed the most uniform morphology, low roughness (6.1 ± 1.0 nm) and high corrosion rate (59.68 ± 1.21 μm/year), and also it provided acceptable radiopacity (~6%) compared to other conditions. In this light, W–Fe–Mn–C coating obtained by magnetron co-sputtering of Fe–13Mn-1.2C (400 W) and W (200 W) could be considered as presuming candidate for the development novel radiopaque degradable coatings on biodegradable Fe–Mn based implants. W–Fe–Mn–C coatings at least 10 μm thick would be necessary to achieve visibility. The obtained 4.5 μm thick coatings can be applied on both sides of the Fe–Mn stents to provide optimum radiopacity.

Declaration of competing interest

This manuscript has not been published and is not under consideration for publication elsewhere. The authors do not have conflicts of interest to disclose.

Acknowledgements

The authors would like to thank Dr. Stephane Turgeon, Mrs. Leticia Marin and Mr. Vinicius Sales for their help in this project. This work was partially funded by the Natural Science and Engineering Research Council of Canada (the *Fonds de Recherche du Québec sur les Natures et Technologie)*, the Canada Foundation for Innovation, and the CHU de Québec Research Center (through the *Fonds de Recherche du Québec sur la Santé*).

Appendix A. Supplementary data

Supplementary data to this article can be found online at https://doi.org/10.1016/j.bioactmat.2021.10.022.

References

[1] Y.P. Kathuria, The potential of biocompatible metallic stents and preventing restenosis, Mater. Sci. Eng. 417 (1–2) (2006) 40–48, https://doi.org/10.1016/j.msea.2005.11.007.
[2] S. Loffredo, H. Hermawan, M. Vedani, D. Mantovani, Absorbable Metals for Cardiovascular Applications, second ed., vol. 2017, Elsevier Ltd., 2019.
[3] J. Bennett, Q. De Hemptinne, K. McCutcheon, Magmaris resorbable magnesium scaffold for the treatment of coronary heart disease: overview of its safety and efficacy, Expet Rev. Med. Dev. 16 (9) (2019) 757–769, https://doi.org/10.1080/17434440.2019.1649133. Oct.
[4] C. Rapetto, M. Leoncini, Magmaris: a new generation metallic sirolimus-eluting fully bioresorbable scaffold: present status and future perspectives, J. Thorac. Dis. 9 (Suppl 9) (2017) S903–S913, https://doi.org/10.21037/jtd.2017.06.34. Oct.

[5] H. Li, Y. Cong, Y. Zheng, L. Cui, In vitro investigation of NiTiW shape memory alloy as potential biomaterial with enhanced radiopacity, Mater. Sci. Eng. C 60 (2016) 554–559, https://doi.org/10.1016/j.msec.2015.12.006.
[6] C. Park, S. Kim, H.E. Kim, T.S. Jang, Mechanically stable tantalum coating on a nano-roughened NiTi stent for enhanced radiopacity and biocompatibility, Surf. Coating. Technol. 305 (2016) 139–145, https://doi.org/10.1016/j.surfcoat.2016.08.014.
[7] H. Hermawan, Updates on the research and development of absorbable metals for biomedical applications, Progress in Biomaterials 7 (2) (2018) 93–110, https://doi.org/10.1007/s40204-018-0091-4.
[8] J. He, et al., Advances in Fe-based biodegradable metallic materials, RSC Adv. 6 (2016) 112819–112838, https://doi.org/10.1039/C6RA20594A.
[9] B.D. Cullity, Elements of X-Ray Diffraction, second ed., Addison-Wesley Publishing Company, Inc., 2001 https://doi.org/10.1021/ed034pA178.
[10] J.H. Hubbell, S.M. Seltzer, "X-Ray Mass Attenuation Coefficients," Radiation Physics Division, PML, NIST, 1996. https://physics.nist.gov/PhysRefData/XrayMassCoef/ElemTab/z73.html. (Accessed October 2020). accessed.
[11] S. Schewe, D.A. Glocker, Coatings for Radiopacity, Scrivener Publishing LLC, 2016, pp. 115–130, https://doi.org/10.1002/9781119308713.ch4.
[12] S.M.H. Garrett Harmon, Tungsten-loaded SMP foam nanocomposites with inherent radiopacity and tunable thermo-mechanical properties, Polym. Adv. Technol. 27 (2016) 195–203. https://doi-org.acces.bibl.ulaval.ca/10.1002/pat.3621.
[13] Z.E. Sánchez-Hernández, M.A. Domínguez-Crespo, A.M. Torres-Huerta, E. Onofre-Bustamante, J. Andraca Adame, H. Dorantes-Rosales, Improvement of adhesion and barrier properties of biomedical stainless steel by deposition of YSZ coatings using RF magnetron sputtering, Mater. Char. 91 (2014) 50–57, https://doi.org/10.1016/j.matchar.2014.02.007.
[14] M.L. Nascimento, W.D. Mueller, A.C. Carvalho, H. Tomás, Electrochemical characterization of cobalt-based alloys using the mini-cell system, Dent. Mater. 23 (3) (2007) 369–373, https://doi.org/10.1016/j.dental.2006.01.026.
[15] E. Mouzou, et al., In vitro degradation behavior of Fe-20Mn-1.2C alloy in three different pseudo-physiological solutions, Mater. Sci. Eng. C 61 (2016) 564–573, https://doi.org/10.1016/j.msec.2015.12.092.
[16] ASTM G59-97, Standard Test Method for Conducting Potentiodynamic Polarization Resistance Measurements, ASTM International, West Conshohocken, 2009, https://doi.org/10.1520/G0059-97R09.
[17] T. Hoffmann, S. Gugel, O. Beuing, G. Rose, Radiopacity assessment of neurovascular implants, Current Directions in Biomedical Engineering 2 (1) (2016) 533–536, https://doi.org/10.1515/cdbme-2016-0118.
[18] Y. Wang, S.L. Jiang, Y.G. Zheng, W. Ke, W.H. Sun, J.Q. Wang, Effect of molybdenum, manganese and tungsten contents on the corrosion behavior and hardness of iron-based metallic glasses, Mater. Corros. 65 (7) (2014) 733–741, https://doi.org/10.1002/maco.201206740.
[19] L. Song, et al., Porous iron-tungsten carbide electrocatalyst with high activity and stability toward oxygen reduction reaction: from the self-assisted synthetic mechanism to its active-species probing, ACS Appl. Mater. Interfaces 9 (4) (2017) 3713–3722, https://doi.org/10.1021/acsami.6b14754.
[20] S.Y. Jian, Y.R. Chu, C.S. Lin, Permanganate conversion coating on AZ31 magnesium alloys with enhanced corrosion resistance, Corrosion Sci. 93 (2015) 301–309, https://doi.org/10.1016/j.corsci.2015.01.040.
[21] J. Cheng, Y.F. Zheng, In vitro study on newly designed biodegradable Fe-X composites (X = W, CNT) prepared by spark plasma sintering, J. Biomed. Mater. Res. B Appl. Biomater. 101 (4) (2013) 485–497, https://doi.org/10.1002/jbm.b.32783.
[22] G. Ghosh, A. Sidpara, P.P. Bandyopadhyay, Understanding the role of surface roughness on the tribological performance and corrosion resistance of WC-Co coating, Surf. Coating. Technol. 378 (2019), https://doi.org/10.1016/j.surfcoat.2019.125080. October.
[23] Y. Dong, L. Fan, H. Chen, L. Dong, Y. Yin, F. Sun, Corrosion behavior of plasma transferred arc Fe-based coating reinforced by spherical tungsten carbide in hydrochloric acid solutions, J. Wuhan Univ. Technol.-Materials Sci. Ed. 35 (2) (2020) 299–309, https://doi.org/10.1007/s11595-020-2257-x.
[24] ASM International®, "Co-20Cr-15W-10Ni," Materials and Coatings for Medical Devices: Cardiovascular ASM Materials for Medical Devices Database Committee, 2009, pp. 69–73.
[25] D. Maintz, et al., Update on multidetector coronary CT angiography of coronary stents: in vitro evaluation of 29 different stent types with dual-source CT, Eur. Radiol. 19 (1) (2009) 42–49, https://doi.org/10.1007/s00330-008-1132-5.
[26] L.L. Geyer, et al., CT evaluation of small-diameter coronary artery stents: effect of an integrated circuit detector with iterative reconstruction, Radiology 276 (3) (2015) 706–714, https://doi.org/10.1148/radiol.15140427.